Lithium-Ion Transport in Carbon Fibers for Structural Batteries

ADVANCED ENERGY & SUSTAINABILITY RESEARCH
www.advenergysustres.com

Lithium-Ion Transport in Carbon Fibers for Structural Batteries

Richa Chaudhary, Ruben Tavano,* Johanna Xu, and Leif E. Asp**

Structural batteries that unite mechanical integrity with electrochemical function hinge on carbon fiber anodes capable of sustaining efficient lithium transport. Carbon fibers possess unique microstructures and multifunctional demands, yet their lithium transport kinetics remain largely unexplored in the context of structural batteries. Here, diffusion processes and interfacial characteristics are quantified in two intermediate-modulus polyacrylonitrile-based fibers (T800S and T800H), which share identical core microstructures but differ in polymer sizing and electrode architecture. T800S outperforms T800H in liquid electrolyte, delivering higher lithiation capacity (≈295 vs. ≈283 mAh g^{-1}) and lower irreversible loss (31% vs. 36%), consistent with more efficient solid electrolyte interphase (SEI) formation and faster charge-transfer dynamics. Under structural battery electrolyte conditions, both fiber types exhibit suppressed capacity, with diffusion coefficients reduced by up to two orders of magnitude (≈10–13 to ≈10–15 cm^2 s^{-1}), as revealed by galvanostatic intermittent titration and impedance spectroscopy. Elevated charge-transfer resistance and diminished interfacial capacitance further highlight the transport limitations imposed by the biphasic structural electrolyte matrix. The results demonstrate that fiber microstructure governs performance in liquid electrolytes, whereas interfacial chemistry and electrode architecture dominate under structural battery electrolyte operation. This mechanistic framework identifies interface engineering and mesoscale design as key strategies for advancing multifunctional structural energy storage.

1. Introduction

The integration of electrochemical energy storage into load-bearing materials offers a disruptive pathway toward lightweight, space-saving solutions for electric transportation and aerospace systems.[1–3] Structural battery composites—which combine mechanical stiffness with lithium-ion storage capability—have emerged as leading candidates in this domain.[4,5] These multifunctional materials typically feature a layered architecture comprising a carbon fiber negative electrode, a glass fiber separator, and a positive electrode, all embedded within a polymer-based structural battery electrolyte (SBE).[6–9] In such systems, carbon fibers fulfill simultaneous roles as lithium hosts, current collectors, and structural reinforcements.[10–14] Recent advancements in structural battery technology have demonstrated promising electrochemical and mechanical performance, with reported elastic moduli up to 76 GPa and energy densities approaching 30 Wh kg^{-1}.[4,5,15] However, several challenges hinder the optimization of these systems. One critical bottleneck is the significantly lower ionic conductivity of SBEs compared to conventional liquid electrolytes (LEs), which limits lithium-ion transport and leads to reduced specific capacities.[16] While this limitation is widely acknowledged, a detailed mechanistic understanding of lithium-ion diffusion within structural electrodes—particularly in the presence of SBE—remains lacking.

Carbon fibers derived from polyacrylonitrile (PAN) are commonly used in these systems due to their favorable strength-to-weight ratios and semi-disordered carbon structures that support lithium storage. Early studies established a strong correlation between microstructure and electrochemical performance, with PAN-based fibers outperforming pitch-based alternatives.[17,18] Among PAN-derived fibers, intermediate modulus (IM) variants exhibit improved lithium storage capacity and cycling reversibility compared to high modulus (HM) fibers.[19,20] This is primarily due to their partially turbostratic and amorphous microstructures, which promote more uniform lithium insertion. High-resolution structural characterizations have shown that IM fibers lithiate in a manner akin to amorphous carbon, while HM fibers follow a graphite-like staging mechanism that is often disrupted by extended crystalline domains and associated defects.[21] These crystalline imperfections are

R. Chaudhary, R. Tavano, J. Xu, L. E. Asp
Department of Industrial and Materials Science
Chalmers University of Technology
Hörsalsvägen 7B, Göteborg 41258, Sweden
E-mail: richac@chalmers.se; ruben.tavano@chalmers.se; leif.asp@chalmers.se

R. Chaudhary, L. E. Asp
Wallenberg Initiative Material Science for Sustainability
Department of Industrial and Materials Science
Chalmers University of Technology
Hörsalsvägen 7B, Göteborg 41258, Sweden

The ORCID identification number(s) for the author(s) of this article can be found under https://doi.org/10.1002/aesr.202500377.

DOI: 10.1002/aesr.202500377

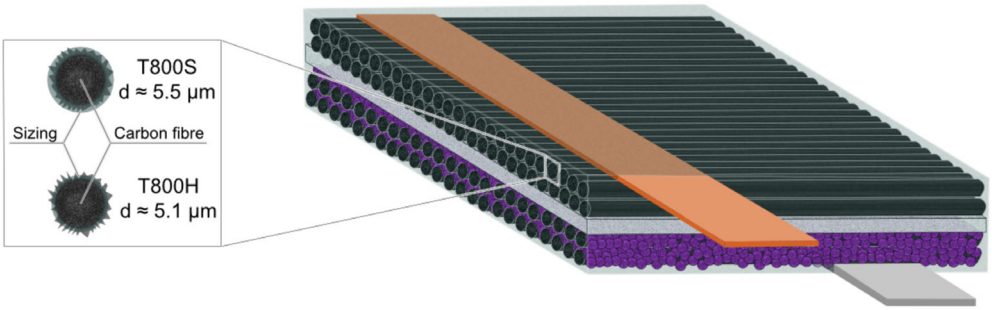

Figure 1. Schematic representation of a structural battery composite architecture and cross-sectional illustration of T800 carbon fibers with differing polymer sizing thicknesses.

believed to limit lithium accessibility and hinder the development of ordered intercalation phases, contributing to the lower capacity observed in HM fibers. Moreover, differences in heteroatom content—such as pyridinic and pyrrolic nitrogen—have been identified as key factors influencing lithium coordination at defect sites, further modulating capacity within IM fibers.[22] Additional work on custom-fabricated fibers has revealed that reducing crystalline content, minimizing crystallite size, and increasing interlayer spacing all enhance lithium storage, albeit at the cost of mechanical properties, underscoring the trade-off between electrochemical and structural performance.[23,24]

Despite these insights, commercial carbon fibers are not optimized for multifunctional use. They are primarily designed for mechanical reinforcement, with precursor chemistries and processing routes that are often undisclosed. Compounding this issue is the presence of a sizing agent, which is a polymer-based surface coating applied to improve fiber-matrix adhesion in composites. While necessary for processing, sizing can influence interfacial electrochemical behavior by affecting lithium-ion accessibility, solid electrolyte interphase (SEI) formation, and charge-transfer resistance. The thickness and composition of the sizing vary between commercial fibers and are rarely reported. These interfacial effects become especially critical when SBE is used, since ionic mobility is already constrained. No differences were however, identified in terms of interfacial mechanical adhesion between different SBEs and differently sized carbon fibers prior to electrochemical cycling.[25] Furthermore, although carbon fibers share structural similarities with graphite—the standard anode in commercial batteries—their electrochemical behavior is shaped by unique microstructural anisotropy, defect distributions, and surface treatments that influence lithium-ion transport.[26–28] Lithium diffusion in graphite has been extensively characterized using techniques such as the galvanostatic intermittent titration technique (GITT), which enabled state-of-charge-dependent mapping of diffusion coefficients and revealed detailed insertion kinetics.[29–32] However, similar high-resolution transport studies in carbon fiber anodes are notably absent. Given their increasing use in structural energy storage, this lack of diffusion data represents a critical knowledge gap. Without such insights, it remains unclear to what extent reduced capacity of carbon fiber electrodes in SBE systems arises from intrinsic transport limitations versus interfacial or structural effects.

To address this, the present study investigates lithium-ion transport kinetics in commercial T800 carbon fibers used as anode materials in structural battery composites. Two fiber variants—T800-SC and T800-HB—were selected based on their identical bulk microstructures but differing sizing thicknesses (**Figure 1**). By combining GITT, electrochemical impedance spectroscopy (EIS), cyclic voltammetry, and galvanostatic cycling in both LE and SBE environments, this study quantifies state-of-charge-dependent lithium diffusion in the carbon fibers and reveals interfacial limitations governed by the electrolyte phase and the fiber's surface coating. For the first time, a comprehensive, quantitative analysis of lithium-ion transport in carbon fiber anodes under structural battery conditions is presented, establishing the critical role of surface and electrolyte interactions in defining rate-limiting processes. These findings offer foundational insight for the rational design of high-performance, multifunctional energy storage materials.

2. Results and Discussion

Surface-dissimilar carbon fibers are evaluated as structural anodes with a focus on their lithium-ion transport properties under conditions representative of structural battery systems. Variation in polymer sizing thickness between T800S and T800H fibers provides a controlled platform to probe the role of fiber–electrolyte interface on SEI formation, lithiation reversibility, and diffusion behavior. SBE, with inherently low ionic conductivity, is used alongside a conventional LE to capture differences in interfacial and bulk transport limitations. In-depth electrochemical analysis enables the quantification of surface-driven differences in charge storage behavior, lithium-ion kinetics, and interfacial resistances. Multiscale analysis reveals how surface composition and morphology shape early-cycle SEI formation and regulate lithium-ion accessibility, particularly under the diffusion-limited regime imposed by the SBE.

2.1. Electrochemical Signatures of Interfacial Reactions Below 0.6 V and Lithium Insertion at 0.5–1.0 V in Carbon Fibers

The surface morphology of the carbon fibers was first examined to establish a connection between structural features and electrochemical behavior. Scanning electron microscope (SEM)2 imaging revealed a ≈0.2 µm thick sizing layer on T800S fibers,

while T800H fibers exhibited exposed cranulations with negligible surface coating (**Figure 2**A,B). This distinct contrast in surface structure provided the rationale for investigating how fiber–electrolyte interactions influence interfacial layer formation and lithium-ion kinetics during cycling. To this end, the effect of surface coating and electrolyte environment on lithium insertion behavior was assessed using cyclic voltammetry (CV), which tracks current response as a function of applied voltage to probe lithium-ion interactions with electrode materials. In a typical scan, a downward peak indicates lithium insertion (reduction during the cathodic scan), while an upward peak corresponds to lithium removal (oxidation during the anodic scan). The shape, position, intensity, and overlap of these peaks provide insight into reaction kinetics, reversibility, and interfacial processes such as electrolyte breakdown and the formation of a passivating surface layer. Figure 2C,D displays CV curves of 1st, 2nd, and 10th cycle at a scan rate of 0.1 mV s^{-1} for two types of carbon fibers—T800S and T800H—in both a conventional LE and an SBE. In both configurations, the first cycle exhibits a pronounced cathodic peak below 0.6 V, attributed to initial electrolyte reduction and the formation of a passivating interfacial layer on the fiber surface. This irreversible reaction is characteristic of SEI formation, which stabilizes the electrode–electrolyte interface in subsequent cycles. The reduction peak occurs at a higher

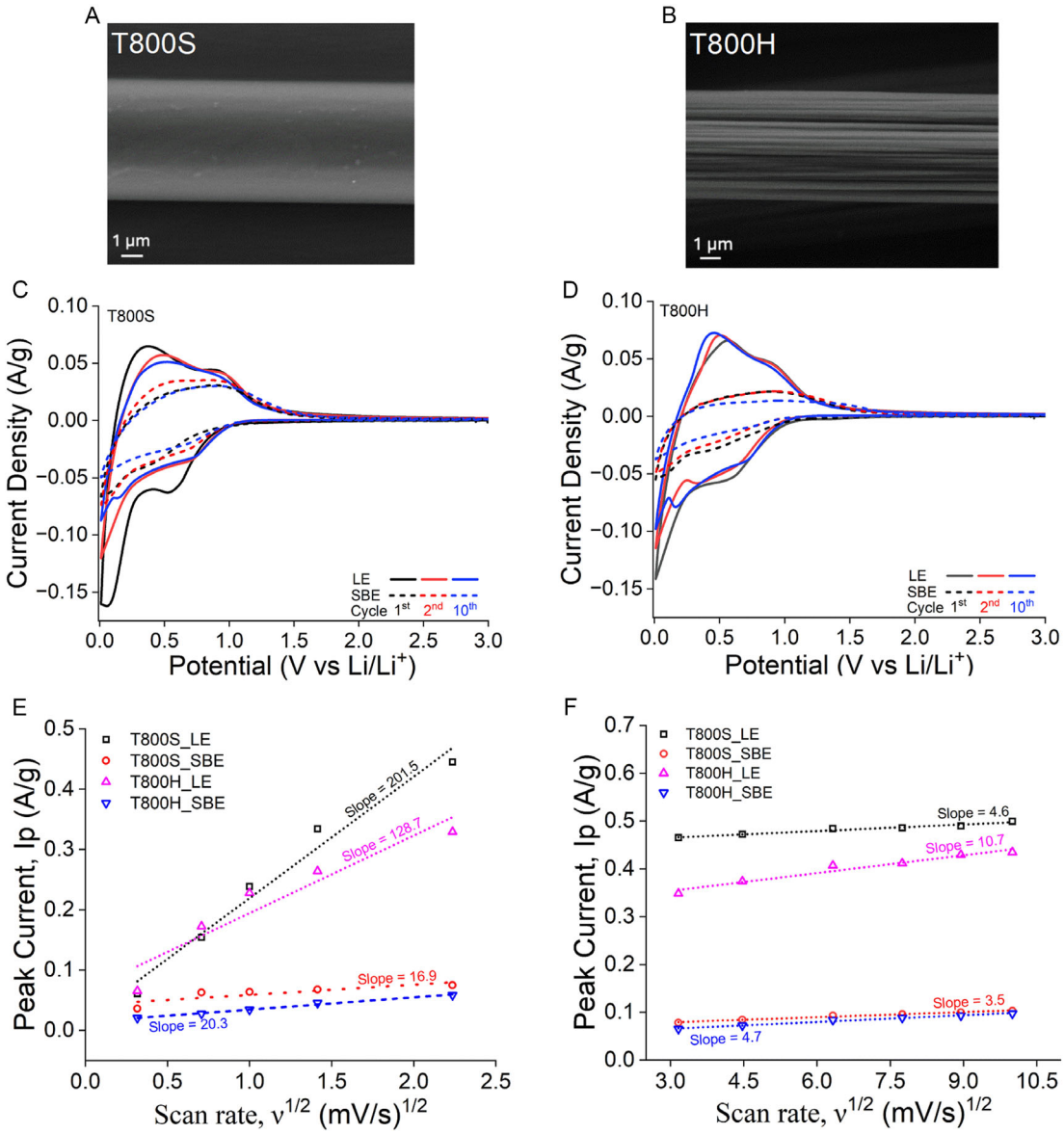

Figure 2. Interfacial layer and lithium insertion behavior in carbon fiber electrodes. A,B) SEM images of T800S and T800H fibers highlighting differences in surface morphology and sizing coverage. C–F) Cyclic voltammograms recorded at 0.1 mV s^{-1} between 0.01 and 3.00 V for T800S and T800H in LE and SBE, illustrating the effects of electrolyte type and surface treatment on early-cycle interfacial reactions and lithium-ion reversibility. E,F) Anodic peak current (I_p) plotted against the square root of scan rate ($\nu^{0.5}$) to assess diffusion behavior at slow (0.1–5 mV s^{-1}) and fast (20–100 mV s^{-1}) sweep rate, respectively.

potential (≈0.60 V) in LE and shifts to ≈0.40 V in SBE, indicating that the kinetics and onset of this interfacial reaction are significantly influenced by the conductivity and composition of the surrounding electrolyte. In later cycles, the diminishing of this initial peak reflects the stabilization of the interfacial layer (Figure S1, Supporting Information). Broad and overlapping anodic peaks between 0.50 and 1.00 V emerge consistently after the first cycle and correspond to lithium extraction from the carbon structure. These features are better defined and more symmetric in LE than in SBE, highlighting improved redox reversibility and faster ion transport in the high-conductivity liquid system.[33–35] In contrast, CV curves in SBE exhibit broader peaks and poorer overlap, indicating slower lithium-ion mobility and less efficient charge transfer, consistent with the lower ionic conductivity of the bicontinuous matrix. The impact of fiber surface characteristics is also evident. T800S fibers, with a thicker polymer sizing, show higher overall current responses compared to T800H in both electrolytes. This difference suggests increased interfacial activity, likely due to altered surface chemistry affecting lithium accessibility and passivation behavior.[36] However, in SBE, the performance of both fibers is more constrained, reflecting the dominant influence of ionic transport limitations.

2.2. Scan Rate-Dependent CV Reveals Diffusion-Controlled Lithium Insertion and Surface-Driven Kinetic Effects

To further investigate lithium-ion transport dynamics and distinguish between kinetic and diffusion limitations, cyclic voltammetry was conducted across a wide range of scan rates (0.1–100 mV s^{-1}) for both T800S and T800H carbon fibers in LE and SBE. These measurements enable evaluation of how efficiently lithium ions access the active material, while also highlighting the influence of electrode–electrolyte interfacial interactions, fiber surface characteristics, and electrolyte conductivity on charge transport and storage behavior. As presented in Figure S2, Supporting Information, increasing the scan rate consistently leads to higher peak currents and broader voltammograms, a characteristic of diffusion-limited behavior.[37] This is an expected behavior based on the Randles–Ševčík relationship, which links peak current (I_P) to the square root of scan rate ($\nu^{0.5}$) for diffusion-controlled redox processes.

$$I_p = 2.69 \cdot 10^5 \cdot n^{1.5} \cdot A \cdot C_{Li} \cdot D_{Li}^{0.5} \cdot m^{-1} \cdot \nu^{0.5} \quad (1)$$

Where I_p indicates the specific peak current, n is the number of electrons transferred, A is the electrode area, D_{Li} is the diffusion coefficient of lithium, C_{Li} is the concentration of Li^+ ions, m is the mass of active material, and ν is the sweep rate.

While all systems follow this trend, the current response is consistently lower for cells containing SBE, reflecting the restricted ionic mobility imposed by the lower conductivity and high tortuosity of the polymer matrix. To quantify these trends, the anodic peak current (I_p) was plotted against $\nu^{0.5}$ in Figure 2E,F, revealing two distinct transport regimes. For slow scan rates (0.1–5 mV s^{-1}), shown in Figure 2E, a high linear slope indicates efficient lithium insertion kinetics. T800S in LE exhibits the highest slope (201.5 mA g^{-1} $(V/s)^{0.5}$), consistent with fast interfacial charge transfer and minimal resistance. In contrast, fibers in SBE show substantially lower slopes—especially for T800H—which suggests limited lithium access and slower kinetics under ionically constrained conditions. At higher scan rates (20–100 mV s^{-1}), shown in Figure 2F, the slope decreases for all samples, as capacitive processes and electrode polarization begin to dominate. Here, T800H-LE demonstrates a slightly higher slope than T800S-LE, implying that the relative influence of sizing on lithium transport diminishes once the surface layer is fully stabilized and the system becomes current-limited. In addition to kinetic analysis, the area enclosed by the CV curves provides a qualitative measure of charge storage capability.[38] T800S-LE exhibits the highest peak currents and largest curve areas, consistent with enhanced lithium-ion accessibility and greater reversible capacity, whereas T800H-SBE shows the lowest response, reflecting suppressed storage performance under ionic transport constraints. The scan rate dependence of peak current follows the Randles–Ševčík relation, confirming that lithium-ion insertion in these electrodes is primarily governed by semi-infinite linear diffusion at low rates. This model links peak current to the square root of scan rate and allows for diffusion coefficients to be inferred from the slope. Notably, under LE conditions, T800S displays steeper slopes than T800H, suggesting that surface sizing promotes more efficient interfacial lithium transport.

However, in the structurally restricted SBE system, ionic conductivity becomes the rate-limiting factor, minimizing the observable influence of surface modification. The in-depth CV analysis guide shows that electrode–electrolyte interactions dominate lithium transport at low rates, where diffusion governs performance, while intrinsic electrode conductivity and structure become more influential at high rates.[39] Moreover, the effect of surface sizing is more pronounced in LE and during slow kinetics, where it affects initial ion access and interfacial charge accumulation. In contrast, performance in SBE is primarily constrained by bulk ionic conductivity, which overshadows surface-related effects.

2.3. Electrochemical Cycling Reveals Sizing-Dependent Lithium Storage Performance in Carbon Fiber Electrodes

Electrochemical cycling offers quantitative insights into lithium storage capacity, reversibility, and long-term stability of carbon fiber electrodes. In the context of structural batteries, where mechanical integrity and ion transport must coexist, understanding how surface modifications such as sizing influence charge–discharge behavior is essential. Key performance indicators, including specific capacity, Coulombic efficiency, and capacity retention, are evaluated across a range of current densities to capture the rate sensitivity and durability of the electrodes under operational conditions. **Figure 3**A,B presents the voltage versus specific capacity profiles for T800S and T800H carbon fibers in LE across increasing current densities of 20, 40, 80, and 160 mA g^{-1}, respectively. These profiles capture the electrochemical behavior during both lithiation and delithiation, which reveals distinct differences in lithium storage performance between the two carbon fiber electrodes, particularly at low current densities where surface-driven phenomena are more prominent. In all cases, T800S electrodes exhibit higher specific capacities than T800H at equivalent rates. The capacity difference

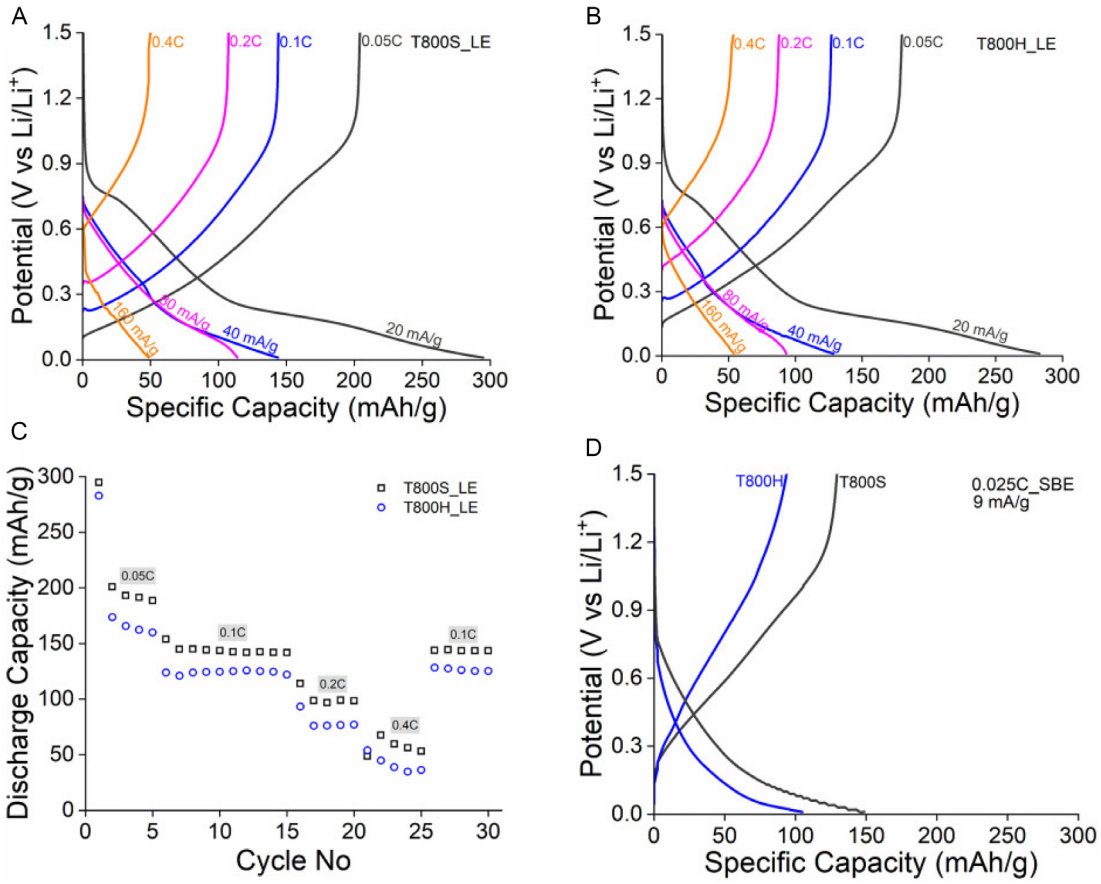

Figure 3. Electrochemical cycling performance of T800 carbon fiber electrodes in liquid and SBEs. A,B) Voltage profiles for galvanostatic charging and discharging as a function of specific capacity at increasing current densities of 20 mA g^{-1} (1st cycle), 40 mA g^{-1} (15th cycle), 80 mA g^{-1} (20th cycle), and 160 mA g^{-1} (25th cycle), respectively, in LE. C) Specific discharge capacity evolution with cycle number across various current densities in LE. D) Voltage profiles of T800S and T800H electrodes in SBE at 9 mA g^{-1}.

is most evident at 20 mA g^{-1} and gradually narrows with increasing current density, suggesting that interfacial effects are more influential at low rates, contribute significantly to the observed performance gap. The voltage profiles retain similar shapes for both fibers, confirming that the lithium insertion mechanism remains consistent, as expected from their shared core microstructure.

This trend is further supported by the first-cycle performance metrics. T800S shows a lower irreversible capacity loss of 31%, compared to 36% for T800H (**Table 1**). These losses primarily reflect lithium consumption during the formation of the SEI.[40] The reduced loss in T800S suggests that its thicker sizing layer may promote more uniform SEI formation, thereby improving interfacial lithium accessibility and enhancing early-cycle efficiency.[41]

Table 1. Electrochemical performance metrics for T800S and T800H carbon fiber electrodes.

Carbon fiber	1st cycle capacity [mAh/g]	15th cycle capacity [mAh/g]	1st cycle loss (%) [mAh/g]	15th cycle Coulombic efficiency [%]	15th cycle capacity retention[a)] [%]
T800S	295	142	91 (31)	100.29	99.72
T800H	283	122	103 (36)	102.83	98.17

[a)]Capacity retention is calculated relative to the second cycle to account for first-cycle losses.

Together, these results highlight the importance of fiber surface characteristics in determining lithium-ion storage behavior, especially under transport-limited conditions. Figure 3C illustrates the evolution of specific capacity across extended cycling at multiple current densities. After initial conditioning, both T800S and T800H fibers display stable capacity profiles, indicating excellent retention over successive cycles. This consistency suggests that once the SEI is established, lithium storage continues with minimal degradation. Correspondingly, the Coulombic efficiency and capacity retention for both carbon fiber electrodes cycled in LE are presented in Figure S3A, Supporting Information. Coulombic efficiency is calculated as the ratio of discharge capacity to charge capacity within the same cycle, reflecting the reversibility of the electrochemical reactions. Capacity retention, meanwhile, is evaluated by comparing the discharge capacity at each cycle to that of the immediately preceding cycle (e.g., cycle 10 relative to cycle 9), providing insight into per-cycle stability under dynamic current conditions. An

initial drop is observed in the first cycle due to irreversible lithium consumption during SEI formation, but efficiencies rapidly approach ≈100% from the second cycle onward, indicating negligible side reactions thereafter. The retention trends plotted alongside show that the electrodes sustain their capacity even under changes in current density. Temporary variations align with rate transitions but recover promptly once the original current is resumed, which highlights the ability of both T800S and T800H fibers to endure rate-induced stress without permanent degradation (Figure S3B, Supporting Information).

2.4. Ionic Limitations in Structural Electrolyte Amplify Surface-Driven Lithiation Behavior

The SBE imposes significantly greater ionic transport limitations than conventional LEs, resulting in markedly lower specific capacities for both T800S and T800H carbon fibers, as shown in Figure 3D. The reduced performance is primarily due to the inherently lower ionic conductivity of the polymer-rich SBE matrix, which hinders lithium-ion mobility and slows the overall lithiation process, particularly at the electrode–electrolyte interface. To isolate these transport effects and accurately evaluate the interfacial contribution of surface sizing, cycling was performed at a low current density of 9 mA g^{-1} (≈0.025 C). This rate minimizes kinetic distortion, allowing meaningful interpretation of steady-state lithium insertion behavior. Moreover, the same electrodes were used for GITT measurements, which require similarly low currents to extract reliable diffusion parameters, further motivating the use of these settings.

Despite identical fiber bulk microstructures, T800S electrodes demonstrate nearly 50% higher specific capacities than T800H under SBE conditions. This discrepancy underscores the impact of surface chemistry: the thicker sizing layer on T800S likely enhances interfacial wettability and ion accessibility, mitigating resistance imposed by the SBE and enabling more effective lithium insertion. Voltage-specific capacity profiles corroborate this interpretation, with T800S electrodes showing more distinct and reversible lithiation/delithiation behavior across the two initial cycles. Differences in electrode architecture may also contribute to the observed disparity. T800S fibers were used in the form of industrially produced thin-ply tapes, composed of a well-spread 12 K tow, ensuring a uniform thickness equal to approximately five fiber diameters. In contrast, T800H electrodes were manually assembled using two layers of 6 K fiber tows, spread by hand to match the total fiber count. The manual spreading may lead to uneven layer thickness, and nonuniform contact with the electrolyte, factors that can introduce variability in lithium-ion accessibility and interfacial impedance.[42] This greater thickness leads to longer ion diffusion pathways, which exacerbate transport limitations in low-conductivity media.

2.5. States of Charge (SOC)-Dependent Diffusion Behavior Highlights Ionic Transport Bottlenecks

Galvanostatic cycling reveals the markedly lower specific capacity in SBE compared with LEs for both carbon fiber types. To rationalize this difference, it is essential to track lithium-ion transport in the two electrolyte systems. The SBE exhibits a biphasic microstructure, comprising a polymer resin and LE in a 1:1 ratio, which governs ion transport within the matrix and across the carbon fibers. Quantification of these transport phenomena is achieved using the GITT. In this method, a constant current pulse is applied for a short duration, followed by an open-circuit relaxation period, allowing the electrode potential to approach equilibrium. The resulting voltage responses are then analyzed to extract diffusion coefficients at different SOC. A representative GITT profile for the charging phase, illustrating the voltage evolution over time, is presented in **Figure 4**A. The corresponding pulse-rest method (Figure 4B**)** yields the steady-state voltage change (ΔV_{rest}) and transient voltage shift (ΔV_{pulse}) required for computing the diffusion coefficient using the modified Fickian model (Equation (2)). The mathematical expression accounts for the cylindrical geometry of the carbon fibers and incorporates key parameters including fiber mass (m_{carbon}), surface area (A_{active}), and molar volume (V_{carbon}), as summarized in Table 3. A linear fit of voltage versus $t^{0.5}$ in a representative pulse (Figure 4C) validates the semi-infinite diffusion assumptions, with R^2 values approaching unity across all fiber types.[43] The complete set of GITT profiles is provided in Figure S4, Supporting Information.

Diffusion coefficients derived during the charging phase at different SOC levels are presented in Figure 4D and Table S1, Supporting Information. Across all electrode–electrolyte configurations, a consistent trend is observed: the diffusion coefficient decreases progressively with increasing SOC. Below 50% SOC, values remain relatively stable, suggesting efficient lithium ingress into available sites. However, above 50% SOC, a marked drop in D_{Li^+} is observed, often by over an order of magnitude, pointing to increased kinetic hindrance as lithium is eliminated from the carbonaceous microstructure. This declining trend is consistent with prior observations in disordered and graphitic carbon systems. Interestingly, the values for T800S and T800H are nearly identical in LE, consistent with their shared microstructure and confirming that intrinsic diffusion is not influenced by the surface sizing layer. In contrast, samples tested in SBE show significantly lower diffusion coefficients at all SOC levels. This difference suggests that the SBE environment introduces an additional transport bottleneck, likely related to its limited ionic conductivity and restricted mobility at the electrode interface. These results imply that while intrinsic carbon fiber diffusion dominates in LE, transport across the solidified interface becomes limiting in structural battery systems. The diffusion coefficients during the discharging phase across various SOC are presented in Figure S5, Supporting Information.

2.6. Structural Electrolyte Constrains Lithium Transport Despite Microstructural Similarity

Although T800 fiber variants exhibit similar lithium diffusion characteristics in LE, the SBE introduces profound performance disparities. In the SBE environment, the D_{Li^+} values for both fibers are consistently one order of magnitude lower than those measured in LE. For example, at 50% SOC, the diffusion coefficient for T800S-LE is $2.51 \cdot 10^{-12}$ cm^2 s^{-1}, while T800S-SBE drops to $4.36 \cdot 10^{-13}$ cm^2 s^{-1}. This significant reduction can be attributed to the intrinsic ionic transport limitations of the SBE matrix

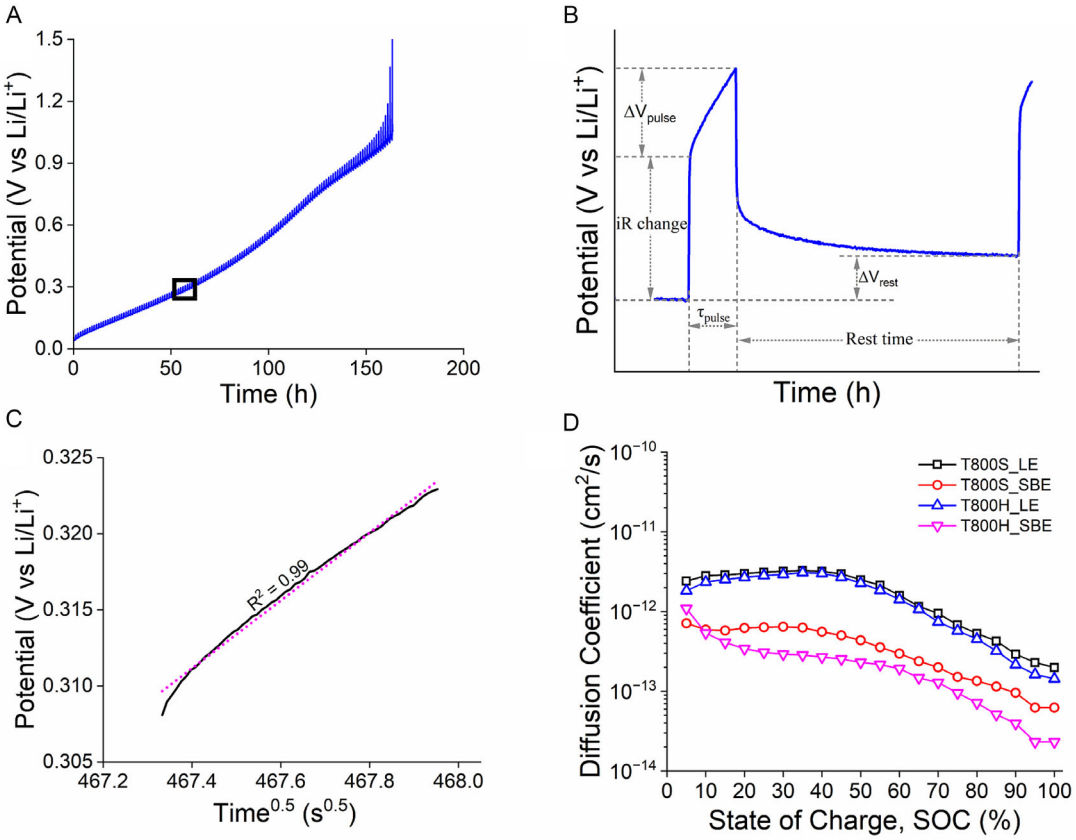

Figure 4. Lithium-ion diffusion behavior during charging assessed by GITT. A) Full voltage profile over time. B) Magnified view of pulse and rest steps. C) Linear fit of potential versus $t^{0.5}$ for diffusion analysis. D) SOC-dependent diffusion coefficients for all samples during charge.

and the constraints it imposes on volumetric expansion of the active material during lithiation.[41,44] The SBE, composed of a polymer-rich phase in glassy state and a LE component, exhibits lower overall ionic conductivity than standard LEs. Moreover, its viscoelastic structure may inhibit the full accommodation of volume changes in the carbon fibers during cycling, thereby restricting interfacial charge transfer and slowing lithium diffusion. The electrochemical environment created by the SBE may also alter the composition and morphology of the SEI, further contributing to sluggish kinetics.

In addition, while the carbon fiber type has minimal effect on intrinsic diffusion in LE, subtle differences emerge in the SBE system. T800S consistently shows slightly higher diffusion coefficients than T800H in SBE across all SOC levels. This minor advantage could stem from the better wettability or ionic accessibility enabled by the thicker sizing layer on T800S, enhancing contact with the polymer electrolyte.[45] However, the dominant limiting factor remains the electrolyte medium itself.

Previous studies on graphite electrodes show similar SOC-dependent diffusion behavior but report values up to two orders of magnitude higher than those observed here. This discrepancy is likely due to the disordered nature of PAN-based carbon fibers, which comprise both amorphous and graphitic domains. These structural features inherently slow lithium transport compared to crystalline graphite but offer enhanced mechanical properties essential for multifunctional structural battery electrodes. Together, these GITT results validate that lithium transport in carbon fiber electrodes is highly sensitive to both SOC and electrolyte phase. While bulk diffusion properties remain consistent across fiber types in LE, interfacial effects dominate in SBE, and these are strongly influenced by the surface coating. This finding underlines the necessity of tailored interfacial engineering for structural battery systems, where electrolyte–electrode coupling governs both electrochemical and mechanical performance. One potential way could be either tailoring the polymer matrix for improved ion mobility or engineering fiber surface treatments that minimize interfacial impedance under quasi-solid-state conditions.

2.7. Impedance Analysis Confirms Ionic Transport Barriers and Supports GITT-Derived Diffusion Trends

EIS was employed to assess the interfacial and transport phenomena of T800S and T800H carbon fiber anodes in both liquid and structural electrolytes, with the goal of elucidating the effects of electrolyte architecture and fiber surface properties on interfacial charge transfer and ion transport (**Figure 5**, Table S2, Supporting Information). For the T800S-based electrodes, Nyquist analysis reveals a pronounced increase in charge-transfer resistance (R_{ct}) from 89.2 Ω in LE to 453.8 Ω in SBE,

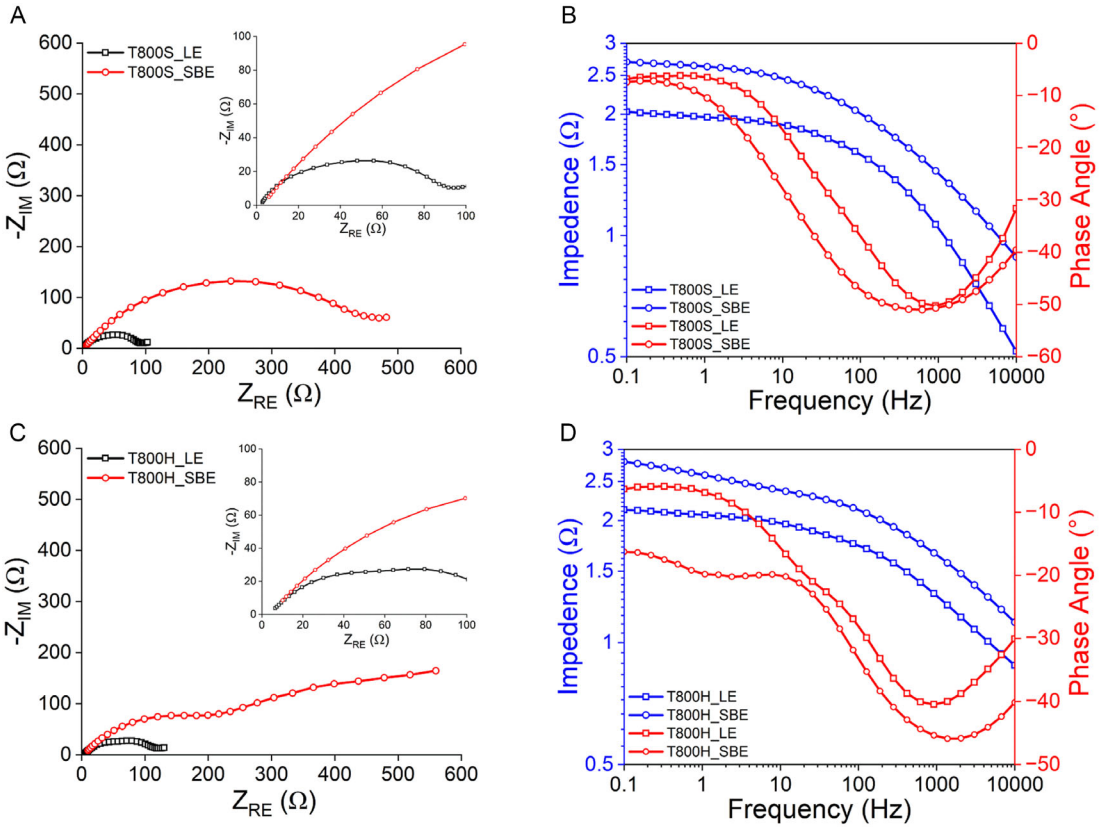

Figure 5. Electrochemical impedance spectra of T800 carbon fiber electrodes in liquid and SBEs. A) Nyquist plots comparing charge transfer and diffusion resistance for T800S electrodes. B) Bode plot showing frequency-dependent impedance magnitude and phase angle for T800S electrodes. C,D) Nyquist and bode plots for T800H electrodes, illustrating the impact of electrolyte environment on interfacial behavior and transport properties.

indicating significantly hindered electrochemical kinetics in the heterogeneous biphasic electrolyte (Figure 5A). The bulk or ohmic resistance (R_s) also increases moderately from 1.66 to 2.85 Ω, likely due to lower ionic conductivity and percolation limitations in the SBE. The depressed semicircle broadens in the SBE condition, reflective of increased interfacial resistance and nonuniform double-layer formation, likely due to poor electrolyte infiltration or limited ionic connectivity at the fiber/electrolyte interface. This is further supported by the Bode plot, which shows an elevated impedance magnitude (|Z|) across the entire frequency spectrum and a shallower phase angle minimum (≈−43° in SBE vs. ≈−52° in LE), consistent with reduced capacitive character and enhanced resistive and diffusive contributions (Figure 5B). The Warburg element (Z_w), representing ion diffusion, also increases markedly (from 11.45 to 37.94 Ω $s^{-1/2}$), further highlighting the sluggish ion transport through the complex SBE network. In comparison, T800H anodes exhibit the same qualitative trends, but with less severe degradation in electrochemical performance upon transition to SBE (Figure 5C). R_{ct} increases from 115.10 Ω (LE) to 203.80 Ω (SBE), and R_s rises from 3.17 to 4.08 Ω. The Nyquist plot reveals a moderate enlargement of the semicircle, suggesting somewhat better interfacial contact or reduced SEI-related impedance relative to T800S. In the Nyquist plot of T800H-LE (Figure 5C), a subtle shoulder followed by a second depressed semicircle becomes apparent. This dual feature likely reflects the presence of multiple overlapping interfacial processes, most notably, a high-frequency arc attributed to interfacial charge-transfer resistance and SEI formation, while the broader mid-frequency arc may reflect lithium-ion migration within the sizing layer or through heterogeneous surface domains. The separation of these processes becomes more distinguishable due to reduced diffusion impedance in the LE system, which lowers the low-frequency tail and reveals finer interfacial resolution. In contrast, under SBE conditions, the dominant impedance response is strongly diffusion-controlled, as evidenced by the long Warburg tail, which masks finer distinctions between interfacial components. Bode analysis similarly shows elevated |Z| and a slight reduction in phase angle minimum (≈−48° in SBE vs. −52° for LE), although the shift is less pronounced than for T800S (Figure 5D). Interestingly, Z_w for T800H shows the largest increase among all samples from 12.28 to 384.50 Ω $s^{-1/2}$, pointing to significant diffusion constraints in the SBE, despite relatively stable charge-transfer kinetics.

The disparity in reaction kinetics between T800S and T800H fibers is likely rooted in differences in effective fiber diameter (5.5 vs. 5.1 µm) and associated polymer sizing thickness. T800S fibers, received in a spread tow configuration, have a thicker sizing layer, which may influence the interface with the electrolyte and limit the active surface area, effects that are

especially detrimental in structurally dense SBEs. This is evidenced by the much higher R_{ct} (453.8 Ω) and the significantly lower magnitude of the constant phase element (CPE) for T800S in SBE, indicating inefficient double-layer formation and poor interfacial connectivity. In equivalent circuit modeling, a CPE is used in place of an ideal capacitor to describe the behavior of the electrode/electrolyte interface when it exhibits nonideal capacitive characteristics, often due to surface roughness, porosity, inhomogeneities, or a distribution of relaxation times across the interface. The CPE value in $F{\cdot}s^{(\alpha-1)}$ provides a measure of the interfacial capacitance, and its magnitude is often correlated with the effective surface area available for double-layer charging. A low CPE, as observed for T800S in SBE ($0.1315{\cdot}10^{-3}$ $F{\cdot}s^{(\alpha-1)}$), suggests either a reduction in the electrochemically active surface or a disruption in the uniformity of ion access across the carbon fiber surface, both of which lead to weakened double-layer capacitance. Additionally, the CPE exponent ($\alpha \approx 0.65$) reflects a clear deviation from ideal capacitive behavior, indicating increased interfacial heterogeneity, likely exacerbated by the structural complexity and limited wetting in the biphasic SBE matrix.

Notably, T800H-SBE exhibits a similarly low CPE magnitude ($0.083{\cdot}10^{-3}$ $F{\cdot}s^{(\alpha-1)}$) and nearly identical α value (0.6563), yet the underlying cause appears distinct. While T800S-SBE is characterized by poor charge transfer (high R_{ct}) and moderate diffusion impedance, T800H-SBE shows a moderate R_{ct} (203.8 Ω) but extremely high Warburg impedance ($Z_w = 384.5\ \Omega\ s^{-1/2}$), suggesting that the low capacitance in this case arises from severely limited ion transport rather than poor electrochemical activity. This contrast illustrates that similar CPE parameters can emerge from fundamentally different interface limitations, whether from restricted electrolyte access or from disrupted charge-transfer pathways. These findings underscore the importance of interpreting CPE behavior in the full context of circuit components and reinforce the critical role of fiber morphology, tow architecture, and sizing chemistry in defining the electrochemical performance of structural battery electrodes.

3. Conclusion

Electrochemical performance in structural battery electrodes is governed by the interplay between carbon fiber surface sizing and electrode architecture. Although T800S and T800H fibers share identical core microstructures, variations in sizing thickness and lamina construction lead to markedly different lithium-ion storage kinetics. The thin-ply, aligned T800S architecture consistently outperforms the twisted-tow T800H, achieving higher lithiation capacity (≈295 mAh g^{-1}) and lower irreversible losses in LE, alongside more defined redox features and enhanced interfacial kinetics. Under SBE conditions, where ionic conductivity is reduced by more than an order of magnitude, both fiber types exhibit diminished capacity, yet T800S retains a ≈50% advantage. GITT reveals diffusion coefficients suppressed by up to two orders of magnitude in SBE compared with LE (from 10^{-13} to 10^{-15} $cm^2\ s^{-1}$), while EIS identifies elevated charge-transfer resistance and reduced interfacial capacitance, highlighting transport bottlenecks imposed by the biphasic matrix. Taken together, the findings demonstrate that in LEs, intrinsic fiber microstructure largely dictates performance, whereas in SBEs, interfacial chemistry and electrode architecture dominate, with even modest differences in sizing or construction influencing the behavior. This establishes a clear mechanistic link between morphology, interface, and electrolyte environment in regulating lithium transport and reversibility. Looking forward, rational engineering of fiber surfaces together with mesoscale architectures emerges as a critical pathway for overcoming transport limitations and enabling multifunctional structural batteries at scale.

4. Experimental Section

Materials: PAN-based carbon fibers of two distinct types were used in this study. T800-40HB-6K fibers were procured from Toray Composite Materials America, Inc. (USA), while T800-50SC-12K fibers were converted into ultrathin unidirectional (UD) tapes by Oxeon AB (Sweden).[46,47] To ensure consistency in fiber count between the two types during electrochemical evaluation, each 12 K segment of T800S was matched with two 6 K segments of T800H, effectively creating equivalent 12 K tow configurations for both electrodes. The linear density of the two fiber types was 0.0053 and 0.0048 g cm^{-1} for T800S and T800H, respectively.

The glass fiber separator (Whatman GF/A, ≈260 µm thick), lithium metal foil (99.9%, 0.75 mm thick), heat initiator 2,2′-azobis(2-methylpropionitrile) (AIBN), lithium bis(trifluoromethanesulfonyl)imide (LiTFSI, anhydrous, 99.99%), propylene carbonate (PC, ≥99%, acid <10 ppm, H_2O <10 ppm), and ethylene carbonate (EC, 99% anhydrous) were all purchased from Sigma Aldrich (USA). The bisphenol-A ethoxylate dimethacrylate (BPAMA, Mn = 540 g mol^{-1}) monomer was generously provided by Arkema Sartomer (France). The copper foil, nickel foil, and silver glue used for the cell assembly were purchased from Ted Pella, Inc. (USA). Two electrolyte systems were prepared with the procured materials. The LE consisted of 1.0 M LiTFSI in a 1:1 weight ratio mixture of EC and PC. The SBE was formulated by mixing the LE with BPAMA in a 1:1 weight ratio and adding 1 wt% AIBN as a thermal initiator.

Methods Fabrication of Structural Negative Electrodes in Half-Cell Configuration: Electrochemical characterization was carried out using two-electrode pouch cells assembled in a half-cell configuration in both liquid and structural electrolytes. The working electrode consisted of a carbon fiber layer, while lithium metal foil was used as both counter and reference electrode. A glass microfiber separator (Whatman GF/A) was placed between the electrodes to ensure electronic insulation. For electrical contact, carbon fiber electrodes were attached to copper current collectors using silver conductive adhesive, whereas the lithium foil was connected to nickel current collectors. Two electrolyte systems were employed: a conventional liquid electrolyte, denoted as LE, and a bicontinuous SBE. In the SBE configuration, the carbon fiber electrodes were vacuum infused with the SBE precursor mixture following a previously established protocol. The infusion was performed under 0.5 bar vacuum, followed by thermal curing at 90 °C for 45 min to form a solidified structural lamina. After curing, the composite electrode was transferred into an argon-filled glovebox, where final cell assembly was performed. The complete cell was sealed in a polyethylene terephthalate (PET):aluminum (Al):polyethylene (PE) pouch film (thicknesses: 12:9:75 µm). To ensure sufficient ionic conduction within the separator, ≈100 µL of supplementary LE was added prior to sealing.

Surface Morphology of Carbon Fibers: The surface morphology of the carbon fibers was examined using a field emission gun scanning electron microscope (FEGSEM) Zeiss LEO-1550 (Zeiss, Germany). Imaging was performed at an accelerating voltage of 5 kV. Owing to the inherent electrical conductivity of the carbon fibers, gold sputter coating was not required for SEM observation.

Electrochemical Testing of Half-Cells: Electrochemical testing was performed using two-electrode pouch cells assembled in a half-cell configuration, where carbon fiber acted as the working electrode and

Table 2. Parameters of T800 carbon fibers used for lithium-ion diffusion coefficient calculations.

Carbon fiber	m_{carbon} [g]	V_{carbon} [cm^3 mol^{-1}]	M_{carbon} [g mol^{-1}]	A_{active} [cm^2]
T800S	$1.67{\cdot}10^{-6}$	6.67	12.01	$8.70{\cdot}10^{-3}$
T800H	$1.50{\cdot}10^{-6}$	6.67	12.01	$7.80{\cdot}10^{-3}$

lithium metal foil served as both counter and reference electrode. To ensure consistency and reproducibility across all measurements, identical pouch cell assemblies were used for each electrochemical technique. CV, GITT, and EIS were carried out using a Bio-Logic SP-300 potentiostat (Bio-Logic, France), while galvanostatic charge/discharge (GCD) cycling was conducted using a Neware CT-4008-5V10mA-164 battery tester (Neware Technology Ltd., China).

CV was performed to investigate lithium-ion insertion kinetics and to evaluate the effect of carbon fiber surface sizing on electrochemical behavior. All measurements were conducted within a potential window of 0.01–3.00 V versus Li/Li$^+$. An initial scan rate of 0.1 mV s^{-1} was applied, followed by successive scans at 0.5, 1, 2, 5, 10, 20, 40, 60, 80, and 100 mV s^{-1} to assess rate-dependent responses.

GCD was conducted to determine the specific capacity, first-cycle loss, voltage profiles, and capacity retention of the carbon fiber electrodes. Cells-containing LE were cycled in a potential window of 0.01–1.50 V versus Li/Li$^+$ at current densities corresponding to 0.05, 0.1, 0.2, and 0.4 C (where 1 C = 372 mAh g^{-1} based on the theoretical capacity of graphite). The mass of the active materials in the negative electrode, the linear density, the currents used, and the corresponding true C-rates are tabulated in **Table 2**. The cycling protocol included five initial cycles at 0.05 C (conditioning), 10 cycles at 0.1 C, five cycles each at 0.2 and 0.4 C, and a final five cycles at 0.1 C. A 2 h rest period was introduced after each charge/discharge step. Two independent samples were tested for each fiber type. Cells using the SBE were cycled over the same voltage window for two cycles at 0.025 C. The specific capacity was calculated from discharge curves using

$$Q = \int \frac{I}{m} dt \tag{2}$$

where Q is the specific capacity (mAh/g), I is the current (A), dt is the time differential (h), and m is the mass of active carbon fiber material (g).

GITT was employed to determine lithium-ion diffusion coefficients in the carbon fiber electrodes as a function of SOC.[48] A constant current pulse corresponding to 0.025 C (based on a theoretical capacity of 372 mAh g^{-1} for graphite) was applied for 10 min, followed by a relaxation period of 1 h under open-circuit conditions to allow for potential stabilization. This pulse-rest sequence was repeated across a voltage range of 0.01 to 1.50 V versus. Li/Li$^+$ for both charging and discharging, with the current direction reversed during the discharge phase. To extract the diffusion coefficients, each pulse and subsequent rest step were automatically identified from the voltage–time profile. The SOC at each point was calculated assuming a quadratic relationship between cell voltage and lithium content, consistent with previous literature.[23,24] The first and last three cycles were excluded from the analysis to avoid artifacts from incomplete relaxation. Lithium-ion diffusion coefficients (D_{Li^+}) were calculated using Fick's second law, assuming semi-infinite diffusion conditions with a formula adapted from Park et al., for cylindrically shaped active material with lithium ions extracted (inserted) during the charging (discharging) phase.[49–51]

$$D_{Li^+}(SOC) = \frac{4}{\pi \cdot \tau_{pulse}} \times \left(\frac{m_{carbon} \cdot V_{carbon}}{M_{carbon} \cdot A_{active}}\right)^2 \times \left(\frac{\Delta V_{rest}(SOC)}{\Delta V_{pulse}(SOC)}\right)^2 \tag{3}$$

where τ_{pulse} is the duration of the current pulse, m_{carbon} is the mass of a single carbon fiber in the carbon fiber tow, V_{carbon} is the molar volume of the carbon fibers, M_{carbon} is the molar mass of the carbon fibers, A_{active} is the total surface area that the lithium ions diffuse through, ΔV_{rest} is the steady-state potential change (associated to the rest steps), and ΔV_{pulse} is the potential change for the charge/discharge pulses neglecting the iR changes (associated to the pulse steps). To improve accuracy, the final reported value at each SOC was determined by averaging the three closest diffusion coefficients. The used parameters for the carbon fibers are shown in **Table 3**.

Table 3. Average active material mass and corresponding applied currents for carbon fiber negative electrodes during electrochemical cycling in LE at different C-rates. The number in parenthesis indicates the true C-rate corresponding to the applied current.

Carbon fiber	Mass [g]	Current at 0.05 C (True C-rate) [mA]	Current at 0.1 C (True C-rate) [mA]	Current at 0.2 C (True C-rate) [mA]	Current at 0.4 C (True C-rate) [mA]
T800S	0.021	0.39 (0.10)	0.78 (0.26)	1.56 (0.75)	3.13 (2.74)
T800H	0.019	0.35 (0.12)	0.71 (0.30)	1.41 (0.94)	2.83 (3.96)

EIS was employed to evaluate internal resistance and interfacial characteristics across different electrode and electrolyte configurations. Measurements were conducted over a frequency range of 100 kHz to 100 mHz, using an AC perturbation amplitude of 10 mV.

Supporting Information

Supporting Information is available from the Wiley Online Library or from the author.

Acknowledgements

R.C. and R.T. contributed equally to this work. The authors gratefully acknowledge financial support from the Wallenberg Initiative Materials Science for Sustainability (WISE), funded by the Knut and Alice Wallenberg Foundation (Dnr LiU-2023-00139), 2D TECH VINNOVA Competence Center (Ref. 2019-00068), and the Office of Naval Research (ONR - USA, Ref. N62909-22-1-2037).

Conflict of Interest

The authors declare no conflict of interest.

Data Availability Statement

The data that support the findings of this study are available from the corresponding author upon reasonable request.

Keywords

electrochemical kinetics, galvanostatic intermittent titration technique, interfacial resistance, lithium-ion transport, structural batteries

Received: September 11, 2025
Revised: November 26, 2025
Published online:

[1] C. A. Aubin, B. Gorissen, E. Milana, P. R. Buskohl, N. Lazarus, G. A. Slipher, C. Keplinger, J. Bongard, F. Iida, J. A. Lewis, R. F. Shepherd, *Nature* **2022**, *602*, 393.
[2] T. Jin, G. Singer, K. Liang, Y. Yang, *Mater Today* **2023**, *62*, 151.
[3] B. J. Hopkins, J. W. Long, D. R. Rolison, J. F. Parker, *Joule* **2020**, *4*, 2240.
[4] L. E. Asp, K. Bouton, D. Carlstedt, S. Duan, R. Harnden, W. Johannisson, M. Johansen, M. K. G. Johansson, G. Lindbergh, F. Liu, K. Peuvot, L. M. Schneider, J. Xu, D. Zenkert, *Adv. Energy Sustain Res.* **2021**, *2*, 2000093.
[5] R. Chaudhary, J. Xu, Z. Xia, L. E. Asp, *Adv. Mater.* **2024**, *36*, 2409725.
[6] N. Ihrner, M. Johansson, *J. Appl. Polym. Sci.* **2017**, *134*.
[7] L. M. Schneider, N. Ihrner, D. Zenkert, M. Johansson, *ACS Appl. Energy Mater.* **2019**, *2*, 4362.
[8] S. Duan, M. Cattaruzza, V. Tu, R. M. Auenhammer, R. Jänicke, M. K. G. Johansson, F. Liu, L. E. Asp, *Commun Mater* **2023**, *4*, 49.
[9] R. Tavano, M. Spagnol, N. Al-Ramahi, R. Joffe, J. Xu, L. E. Asp, *Polymer* **2024**, *312*, 127646.
[10] L. E. Asp, E. S. Greenhalgh, *Compos. Sci. Technol.* **2014**, *101*, 41.
[11] L. E. Asp, M. Johansson, G. Lindbergh, J. Xu, D. Zenkert, *Funct. Compos. Struct.* **2019**, *1*, 042001.
[12] W. Johannisson, D. Zenkert, G. Lindbergh, *Multifunct. Mater.* **2019**, *2*, 035002.
[13] R. Chaudhary, A. Chetry, J. Xu, Z. Xia, L. E. Asp, *Adv. Sci.* **2024**, *11*, 2404012.
[14] K. Bouton, L. Schneider, D. Zenkert, G. Lindbergh, *Compos. Sci. Technol.* **2024**, *256*, 110728.
[15] M. S. Siraj, S. Tasneem, D. Carlstedt, S. Duan, M. Johansen, C. Larsson, J. Xu, F. Liu, F. Edgren, L. E. Asp, *Adv. Ener. Sust. Res.* **2023**, *4*, 2300109.
[16] M. Cattaruzza, Y. Fang, I. Furó, G. Lindbergh, F. Liu, M. Johansson, *J. Mater. Chem. A* **2023**, *11*, 7006.
[17] W. Ruland, *Adv. Mater.* **1990**, *2*, 528.
[18] J. F. Snyder, E. L. Wong, C. W. Hubbard, *J. Electrochem. Soc.* **2009**, *156*, A215.
[19] M. H. Kjell, E. Jacques, D. Zenkert, M. Behm, G. Lindbergh, *J. Electrochem. Soc.* **2011**, *158*, A1455.
[20] J. Hagberg, S. Leijonmarck, G. Lindbergh, *J. Electrochem. Soc.* **2016**, *163*, A1790.
[21] G. Fredi, S. Jeschke, A. Boulaoued, J. Wallenstein, M. Rashidi, F. Liu, R. Harnden, D. Zenkert, J. Hagberg, G. Lindbergh, P. Johansson, L. Stievano, L. E. Asp, *Multifunct. Mater.* **2018**, *1*, 015003.
[22] M. Johansen, C. Schlueter, P. L. Tam, L. E. Asp, F. Liu, *Carbon* **2021**, *179*, 20.
[23] J. Xu, C. Creighton, M. Johansen, F. Liu, S. Duan, D. Carlstedt, P. Mota-Santiago, P. Lynch, L. E. Asp, *Carbon* **2023**, *209*, 117982.
[24] R. Tavano, J. Xu, C. Creighton, F. Liu, B. Dharmasiri, L. C. Henderson, L. E. Asp, *Batter. Supercaps* **2024**, *7*, e202400110.
[25] J. Xu, W. Johannisson, M. Johansen, F. Liu, D. Zenkert, G. Lindbergh, L. E. Asp, *Compos. Sci. Technol.* **2020**, *188*, 107962.
[26] M. Endo, Y. Nishimura, T. Takahashi, K. Takeuchi, M. S. Dresselhaus, *J. Phys. Chem. Solids* **1996**, *57*, 725.
[27] M. Inaba, H. Yoshida, Z. Ogumi, T. Abe, Y. Mizutani, M. Asano, *J. Electrochem. Soc.* **1995**, *142*, 20.
[28] K. Dai, Z. Wang, G. Ai, H. Zhao, W. Yuan, X. Song, V. Battaglia, C. Sun, K. Wu, G. Liu, *J. Power Sources* **2015**, *298*, 349.
[29] I. O. Santos-Mendoza, J. Vázquez-Arenas, I. González, G. Ramos-Sánchez, C. O. Castillo-Araiza, *International Journal of Chemical Reactor Engineering* **2019**, *17*.
[30] C.-H. Chen, F. Brosa Planella, K. O'Regan, D. Gastol, W. D. Widanage, E. Kendrick, *J. Electrochem. Soc.* **2020**, *167*, 080534.
[31] A. Nickol, T. Schied, C. Heubner, M. Schneider, A. Michaelis, M. Bobeth, G. Cuniberti, *J. Electrochem. Soc.* **2020**, *167*, 090546.
[32] D. W. Dees, S. Kawauchi, D. P. Abraham, J. Prakash, *J. Power Sources* **2009**, *189*, 263.
[33] G. Liu, Y. Yang, X. Lu, F. Qi, Y. Liang, A. Trukhanov, Y. Wu, Z. Sun, X. Lu, *ACS Appl. Mater. Interfaces* **2022**, *14*, 31803.
[34] Q. Sun, D. Li, J. Cheng, L. Dai, J. Guo, Z. Liang, L. Ci, *Carbon* **2019**, *155*, 601.
[35] H. Wu, L. Wei, W. Li, C. Shi, X. Yao, Q. Fu, H. Li, X. Guo, *Adv. Funct. Mater.* **2024**, *34*, 2403729.
[36] D. Zhou, Z. Liu, X. Lv, G. Zhou, J. Yin, *Electrochim. Acta* **2006**, *51*, 5731.
[37] F. Fu, Y. Yao, H. Wang, G.-L. Xu, K. Amine, S.-G. Sun, M. Shao, *Nano Energy* **2017**, *35*, 370.
[38] T. Liu, W. Wang, M. Yi, Q. Chen, C. Xu, D. Cai, H. Zhan, *Chem. Eng. J.* **2018**, *354*, 454.
[39] Y. Fu, Q. Gan, *J. Solid State Electrochem.* **2023**, *27*, 345.
[40] M. Johansen, M. P. Singh, J. Xu, L. E. Asp, B. Gault, F. Liu, *Carbon* **2024**, *225*, 119091.
[41] M. H. Kjell, T. G. Zavalis, M. Behm, G. Lindbergh, *J. Electrochem. Soc.* **2013**, *160*, A1473.
[42] D. Carlstedt, F. Rittweger, K. Runesson, A. M. Navarro-Suárez, J. Xu, S. Duan, F. Larsson, K.-R. Riemschneider, L. E. Asp, *Compos. Sci. Technol.* **2022**, *220*, 109283.
[43] E. Deiss, *Electrochim. Acta* **2005**, *50*, 2927.
[44] E. Jacques, M. Hellqvist Kjell, D. Zenkert, G. Lindbergh, M. Behm, *Carbon* **2013**, *59*, 246.
[45] D. Li, Q. Lv, C. Zhang, W. Zhou, H. Guo, S. Jiang, Z. Li, *Batteries* **2022**, *8*, 101.
[46] Toray. T800S-Technical-Data-Sheet-1. T800S-Technical Data Sheet. https://www.toraycma.com/wp-content/uploads/T800S-Technical-Data-Sheet-1.pdf (accessed on December 2024).
[47] Toray. T800H-Technical-Data-Sheet-1. T800H-Technical Data Sheet. https://www.toraycma.com/wp-content/uploads/T800H-Technical-Data-Sheet-1.pdf (accessed on December 2024).
[48] W. Weppner, R. A. Huggins, *J. Electrochem. Soc.* **1977**, *124*, 1569.
[49] J. Crank, *The Mathematics Of Diffusion*, Clarendon Press, Oxford **1976**.
[50] J. Kaspar, M. Graczyk-Zajac, R. Riedel, *Electrochim. Acta* **2014**, *115*, 665.
[51] J. H. Park, H. Yoon, Y. Cho, C.-Y. Yoo, *Materials* **2021**, *14*, 4683.